ADVANCED MATERIALS
www.advmat.de

Tin (II) Chloride Salt Melts as Non-Innocent Solvents for the Synthesis of Low-Temperature Nanoporous Oxo-Carbons for Nitrate Electrochemical Hydrogenation

*Xinyue Zheng, Zhihong Tian, Roza Bouchal, Markus Antonietti, Nieves López-Salas, and Mateusz Odziomek**

Carbonaceous electrocatalysts offer advantages over metal-based counterparts, being cost-effective, sustainable, and electrochemically stable. Their high surface area increases reaction kinetics, making them valuable for environmental applications involving contaminant removal. However, their rational synthesis is challenging due to the applied high temperatures and activation steps, leading to disordered materials with limited control over doping. Here, a new synthetic pathway using carbon oxide precursors and tin chloride as a p-block metal salt melt is presented. As a result, highly porous oxygen-rich carbon sheets (with a surface area of 1600 $m^2\ g^{-1}$) are obtained at relatively low temperatures (400 °C). Mechanistic studies reveal that Sn(II) triggers reductive deoxygenation and concomitant condensation/cross-linking, facilitated by the Sn(II) → Sn(IV) transition. Due to their significant surface area and oxygen doping, these materials demonstrate exceptional electrocatalytic activity in the nitrate-to-ammonia conversion, with an ammonia yield rate of 221 mmol $g^{-1}\ h^{-1}$ and a Faradic efficiency of 93%. These results surpass those of other carbon-based electrocatalysts. In situ Raman studies reveal that the reaction occurs through electrochemical hydrogenation, where active hydrogen is provided by water reduction. This work contributes to the development of carbonaceous electrocatalysts with enhanced performance for sustainable environmental applications.

1. Introduction

Nanoporous carbons have come a long way from "simple" sorbents to key materials in energy storage and conversion.[1–4] The traditional nomenclature for such carbons is "activated carbons," a term derived from the top-down chemical etching-based preparation method.[5] However, this methodology lacks control over structural and microstructural properties, leading to limited pore size, loss of mass yield, and corrosion of the original functionality by the activation process. Alternatively, bottom-up approaches rely on the condensation-aromatization of organic molecules or polymers forming a carbonaceous network with predefined structural motifs.[6] In that case, the most flexible strategy to introduce nanopores is salt melt templating.[7,8]

The salt melts provide a highly polar liquid medium for condensation and aromatization of organic species at temperatures too high for conventional liquid solvents. At the same time, they act as structure-directing or templating agents, enabling tuning the pore size distribution in a broader range (micro-, meso-, and macropores).[8–11] The most frequently used salts are inert alkali chlorides, which mostly provide a liquid medium for the carbon formation process.[7] Fechler et al. used $ZnCl_2$ in a eutectic mixture with alkali chlorides, reaching much lower melting points compared to the standard alkali chloride salt melt synthesis (i.e., T_m $ZnCl_2$:NaCl: 270 °C). In addition, Zn cations acted as efficient Lewis acid catalysts, accelerating condensation and dehydration reactions.[12]

X. Zheng, R. Bouchal, M. Antonietti, N. López-Salas, M. Odziomek
Colloid Chemistry Department
Max Planck Institute of Colloids and Interfaces
Am Mühlenberg 1, 14476 Potsdam, Germany
E-mail: mateusz.odziomek@mpikg.mpg.de

The ORCID identification number(s) for the author(s) of this article can be found under https://doi.org/10.1002/adma.202311575

DOI: 10.1002/adma.202311575

Z. Tian
Engineering Research Center for Nanomaterials
Henan University
Kaifeng 475004, P. R. China

N. López-Salas
Sustainable Materials Chemistry
Paderborn University
Warburger Strasse 100, 30098 Paderborn, Germany

Antonietti et al introduced the reactive salt melts, which contained reactive oxidants, like nitrates, adding the activation effect.[13] The list of utilized salt melts for carbon synthesis appears mostly limited to s-block metals chlorides and $ZnCl_2$ representing d-block metals. The empty d-orbitals of transition metals interact with lone pairs and catalyze the thermal condensation of small organic molecules.[14] Although p-block metals have been recognized as valuable catalysts,[15,16] they remain unexplored as salt melts in carbon synthesis. Notably, DFT calculations show that the interaction of p-block metals with the lone p-orbitals of O or N facilitates the electron transfer between them.[17]

Herein, we introduce $SnCl_2$, p-block metal chloride, as a non-innocent salt melt medium to synthesize nanoporous carbons. It has a very low melting point (180 °C, in a eutectic mixture with KCl), exhibits catalytic activity for organic transformations (esterification, allylation, and propargylation reactions),[18–20] and acts as both Lewis acid (empty p-orbital) and Lewis base (free electron pair on another p-orbital). Red carbon (RC), an oligomer of chemical composition $(C_3O_2)_n$, was selected as the model carbon precursor.[21] The high affinity of tin for oxygen and its ability to undergo redox reaction from 2+ to 4+, cause a remarkable effect on the condensation-aromatization process and porosity development. Already at 300 °C, a highly porous oxocarbon structure (658 $m^2\ g^{-1}$) emerged, reaching a value of 1600 $m^2\ g^{-1}$ at 400 °C, which was stable at least to 800 °C.

The fabricated porous carbonaceous materials catalyzed the metal-free nitrate electroreduction to ammonia with a high yield rate of 221 mmol $h^{-1}\ g^{-1}$, high Faradaic efficiency (FE) of 93.4%, well overpassing other carbon catalysts, even some carbon-supported metal catalysts.[22,23] The detailed investigation unravels the role of oxygen functionalities and conductive carbonaceous framework in efficient binding of nitrate ions through hydrogen bonding, which is reflected by high nitrate adsorption capacity. The resulting preconcentration on the oxocarbon surface allows for efficient nitrate removal even from low-concentration solution, and in consequence, effective removal of nitrates. In situ Raman analysis revealed the mechanism that the nitrate reduction occurs through electrochemical hydrogenation, a mechanism up to now typical for metal-based catalysts.[24–26] Therefore, the obtained oxocarbons are promising catalysts for water purification from nitrate contaminants without the danger of corrosion and dissolution of metal electrodes contributing to water contamination,[27] and bringing nitrate back to the nitrogen cycle, mitigating the necessity for ammonia production through energy-intensive Haber–Bosh process.[28]

2. Results and Discussions

2.1. The Effect of $SnCl_2$/KCl Salt Melt

RC is an oligomeric, semiconducting material derived from carbon suboxide monomer, with empirical formula $(C_3O_2)_x$. Its rigid structure features a polyacetylene chain backbone flanked by —OC(O)— groups (**Figure 1a**). This conjugated planar structure and the absence of structure terminating and inactive C—H bonds are attractive for synthesizing carbonaceous materials at milder conditions.[21,29] In order to minimize the temperature required for thermal condensation and the formation of a rigid, more organized carbon network, RC was thermally treated in $SnCl_2$/KCl salt melt (SnK) as its melting point is lower than the onset of RC decomposition and cross-linking (Figure S1, Supporting Information). In addition, Sn(II) can act as both Lewis acid and base providing specific interaction between the p-block metal and the oxygen atoms in RC.[15,16] For comparison, the RC was also thermally treated in typical salt melts such as $ZnCl_2$/KCl (ZnK) and LiCl/KCl (LiK). In each case, the RC was thoroughly ground with the eutectic mixtures, heated in the oven under an N_2 atmosphere at different temperatures, and repeatedly washed with 1 M HCl (Figure 1a). The obtained samples were named RC-*MK*-*T* (*M* is salt: Sn, Zn, Li; *T* is the thermal treatment temperature). The properties of the materials obtained at 400 and 600 °C are depicted in Figure 1 and Figures S2–S8, Supporting Information, and summarized in Table S1, Supporting Information.

Undoubtedly, SnK salt melt has the most significant impact on the thermal condensation process of RC. Already at 400 °C, the obtained material contains 79 wt% of carbon atoms (describing the extent of condensation-aromatization), more than those obtained in LiK and ZnK salt melts (68 and 73 wt%, respectively) (Figure 1b). At the same time, RC-SnK-400 had the largest synthesis yield of 44% compared to 42% and 36% obtained for RC-LiK-400 and RC-ZnK-400, respectively (Table S1, Supporting Information). The higher carbon content indicates that condensation occurs at a lower temperature in SnK than in other salt melts. Although one could expect higher reaction rates in the presence of Zn^{2+}, a strong Lewis acid, it is Sn^{2+} that shows higher catalytic activity. We discuss that in the following parts of the manuscript.

X-ray diffraction (XRD) patterns of the samples calcined at 400 °C showed no crystalline features, thus demonstrating the loss of the translational order of the initial oligomeric precursor (Figure S2, Supporting Information). However, scanning electron microscopy (SEM) image of RC-SnK-400 revealed the formation of large 2D sheets at 400 °C (Figure 1c). They were made solely of carbon and oxygen, as confirmed by energy-dispersive X-ray (EDX) mapping (Figure 1d). Contrarily, RC-LiK-400 and RC-ZnK-400 consisted of irregular particles (Figure S3, Supporting Information). The enhanced $SnCl_2$-assisted condensation of RC also led to an unexpectedly high specific surface area (SSA) of 1600 $m^2\ g^{-1}$ at temperatures as low as 400 °C, determined by Brunauer–Emmett–Teller (BET) analysis from N_2 sorption isotherms at 77 K (Figure 1d). In contrast, RC-ZnK-400 developed only 600 $m^2\ g^{-1}$, while RC-LiK-400 had a minor influence on SSA compared to RC calcined without salt melt (Figure S4, Supporting Information). The pore size distribution calculated by quenched solid density functional theory (QSDFT) showed that the major pore contribution of RC-SnK-400 is centered around 2.2 nm. Moreover, the calcination at higher temperatures (600 °C) did not cause dramatic changes in the crystallinity, morphology, and surface areas (1558, 656, and 523 $m^2\ g^{-1}$ for RC-SnK-600, RC-ZnK-600, and RC-LiK-600) (Figures S5–S7, Supporting Information).

The results show that Sn(II) ions have the most substantial impact on condensation. Sn(II) can behave as both Lewis base (because of free electrons at $6sp^2$), and Lewis acid owing to available free p orbitals. Despite the absence of empty d-orbitals, Sn(II) promotes the reductive deoxygenation process, primarily due to the strong interaction between tin and oxygen.[30] The hard-soft acid-base (HSAB) theory is commonly employed to qualitatively compare the strength of acid-base interactions. While oxygen

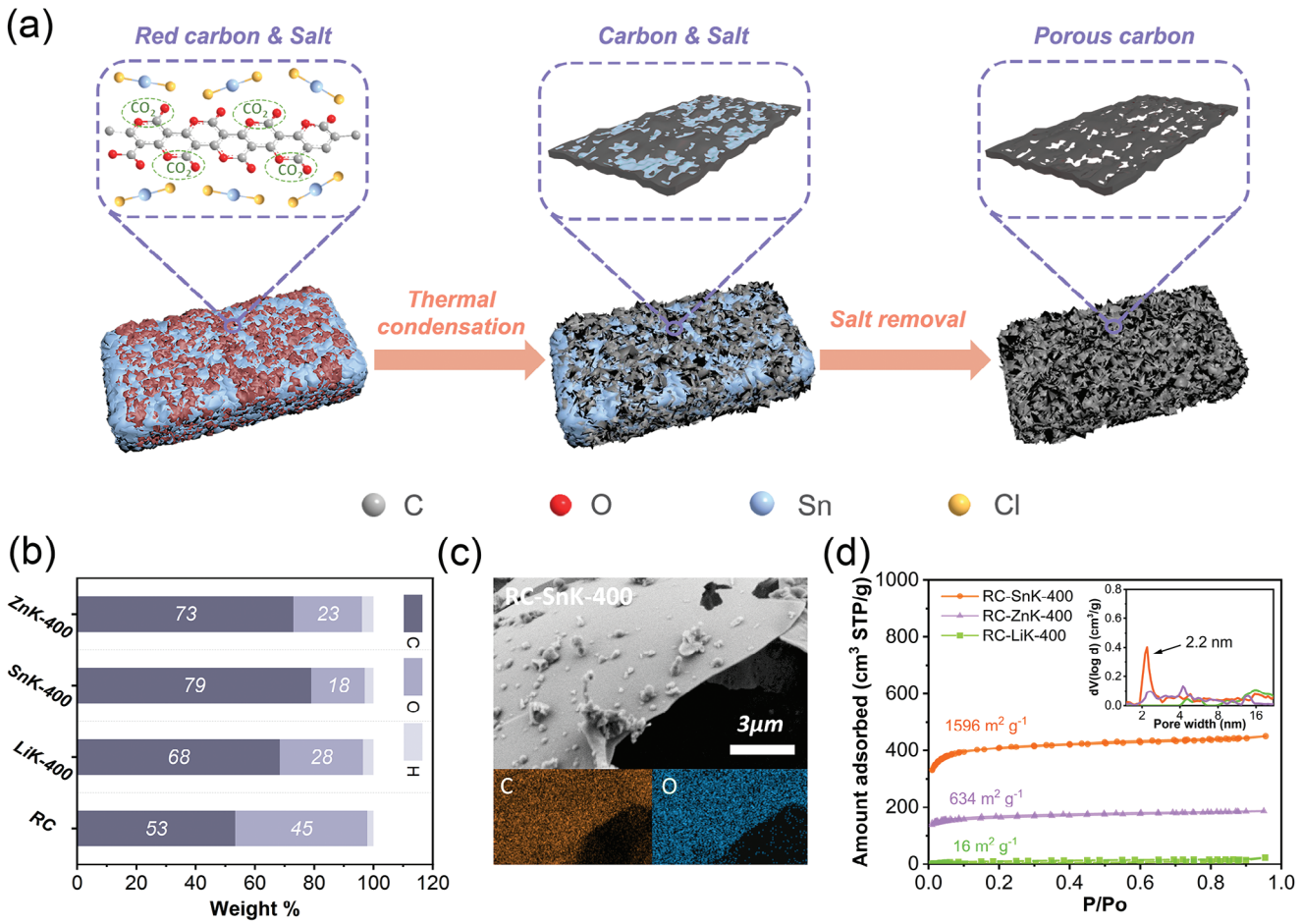

Figure 1. The thermal condensation of RC in different salt melts. a) Scheme of the synthesis process by salt melt method; b) Chemical composition obtained from elemental chemical analysis; c) SEM image and EDX mapping of carbon (orange) and oxygen (blue) atoms in RC-SnK-400; d) N_2 adsorption–desorption isotherms at 77 K of RC-SnK-400, RC-LiK-400, and RC-ZnK-400 (inset: corresponding pore-size distributions calculated by QSDFT model from adsorption branch).

atoms are considered hard bases, both Zn^{2+} and Sn^{2+} are classified as borderline Lewis acids pointing at a little difference in the view of HSAB theory.[31] However, Kepp[32] demonstrated that oxophilicity (the ability to bind to oxygen and remove it from other elements) is not firmly correlated to the hardness of an element. Through calculations of relative oxophilicity based on M—O bond enthalpies, he revealed that Sn exhibits twice the oxophilicity of Zn. The enhanced binding of Sn to O accounts for the increased condensation, lower oxygen content in the final materials, and consequently, a higher surface area. Despite lacking empty d-orbitals, Sn(II) favors the reductive deoxygenation process resulting from the strong interaction between tin and oxygen.

2.2. The Mechanism of Cross-Linking and Pore Formation

To investigate the role of Sn(II) ions in the formation of RC-derived oxocarbons, we followed the condensation process by ex situ XRD and Fourier-transform infrared (FTIR) spectroscopy analyses. In order not to saturate the XRD and FTIR signals with an excess of $SnCl_2$ and KCl (which act as a mere "spectator" solvent component in the process), RC and $SnCl_2$ were mixed in a weight ratio of 1:1. The mixture was ground manually, heat-treated for 2 h under nitrogen at different temperatures (100, 200, and 300 °C), and analyzed without further purification. **Figure 2a,b** depicts the XRD patterns and the FTIR spectra of RC-$SnCl_2$ mixtures before and after calcination at the indicated temperatures. Additionally, the spectra are compared to those of $SnCl_2$ alone and $SnCl_2$ heat-treated at 200 °C under an N_2 atmosphere ($SnCl_2$-200).

The as-utilized $SnCl_2$ was a sesquihydrate, as all peaks matched the $SnCl_2$•1.5 H_2O phase (JCPDS 04-016-0301). The XRD pattern of the ground mixture (RC-$SnCl_2$) differed from the patterns of the initial individual components. As $SnCl_2$ is a hygroscopic compound, the observed XRD patterns are complex and could correspond to tin chloride at various hydration levels.[33] The RC peaks vanished due to a reaction with $SnCl_2$ or a much stronger scattering cross-section of Sn atoms than C atoms. Some peaks could be assigned to anhydrous (JCPDS 04-007-3801) and hydrous (JCPDS 04-016-0301) $SnCl_2$, as shown in Figure 2a. The rest of the peaks remain unknown, suggesting

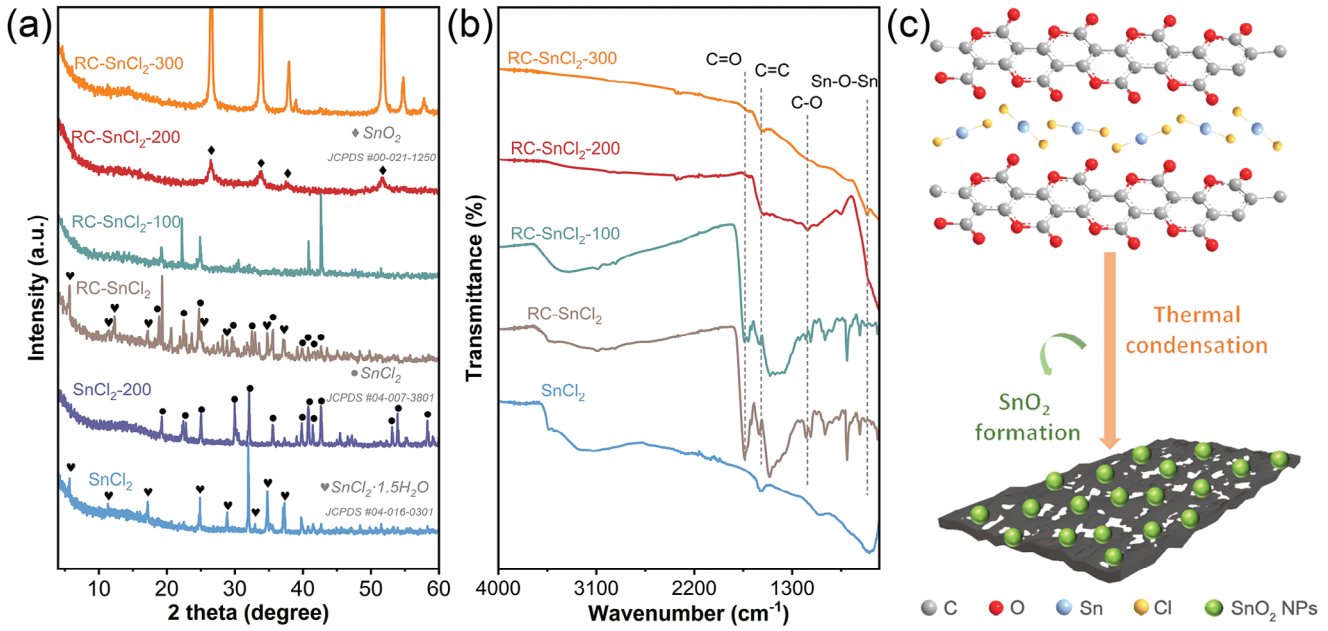

Figure 2. The Sn(II) effect during thermal condensation. a) XRD patterns and b) FTIR spectra of RC-$SnCl_2$, RC-$SnCl_2$-100, RC-$SnCl_2$-200, RC-$SnCl_2$-300, and RC-$SnCl_2$-400 (with $SnCl_2$ and $SnCl_2$-200 for comparison); c) The schematic picture of pore formation mechanism.

a possible mechanochemical reaction between both species already during the grinding process.

After heat treatment at 100 °C, a different set of peaks appeared, likely due to the dehydration of the as-received $SnCl_2$. Unfortunately, at this temperature, we were unable to unambiguously assign these peaks. A stable phase emerged at 200 °C, and its XRD peaks increased in intensity at 300 °C, displaying the characteristic pattern of the tetragonal SnO_2 phase (JCPDS 00-021-1250). The relatively broad peaks indicate the formation of SnO_2 nanoparticles. When heating as-utilized $SnCl_2$ at 200 °C ($SnCl_2$-200) in a blank experiment, the pattern typical of dehydrated $SnCl_2$ (JCPDS 04-007-3801) was observed without forming oxide phases. This suggests that the O atoms in SnO_2 originate solely from RC. In other words, Sn(II) first binds (likely during the grinding step) and intercepts O atoms from RC upon mild heating. This process involves the oxidation of Sn(II) to Sn(IV) and the simultaneous reduction of C atoms, which occurs through cross-linking neighboring RC ribbons. This redox reaction appears to be the key factor facilitating network formation, particularly when compared to Zn ions.

The FTIR analysis, performed similarly, is more sensitive toward the chemical evolution of RC but stays in full agreement with XRD analysis (Figure 2b). The grinding of both components does not destroy the RC, as the FTIR spectra have the same peak structure before and after grinding with $SnCl_2$ (Figure S8, Supporting Information). As grinding with $SnCl_2$ influences the crystallographic structure of RC but not the vibration structure of chemical bonds, we speculate that $SnCl_2$ intercalates between the RC ribbons. The chemical structure does not change upon heating to 100 °C, but at 200 °C the C═O bond centered at ≈1740 cm^{-1} disappears, accompanied by the cross-linking of the ribbons. Concomitantly, a peak at 610 cm^{-1} corresponding to the Sn—O—Sn bond appears, confirming the formation of SnO_2 at the expense of C═O bonds already at 200 °C (Figure 2b).

In summary, the interaction between RC and $SnCl_2$ takes place already during the grinding stage. The crystallographic structure of RC is disrupted while the chemical structure remains intact. This implies that $SnCl_2$ intercalates between RC ribbons, which may account for the appearance of unidentified XRD peaks. Upon thermal treatment, tin atoms from $SnCl_2$ intercept oxygen atoms from RC forming SnO_2 nanoparticles and forcing cross-linking between RC ribbons. At the same time, formed SnO_2 nanoparticles act as in situ-formed hard templates, contributing to the stabilization of uniform pores. SnO_2 nanoparticles were observed by transmission electron microscopy (TEM), and their size of about 2 nm (Figure S9, Supporting Information) corresponds well to the pore size distribution measured by nitrogen sorption. Figure 2c illustrates the pore formation mechanism. Such pore formation mechanism explains the stability of pore structure (pore size, SSA, etc.) upon further heat treatment at higher temperatures, as presented in the next section.

2.3. The Influence of Temperature on Properties of Derived Carbons

In the next step, RC was further condensed in SnK at temperatures between 300 and 800 °C, then acid-washed to probe the effect of the temperature on the properties of derived materials (Table S2, Supporting Information). Each sample contained residual Sn below 0.2 wt% after acid washing, significantly lower than the residual Zn content reported in Zn-based salt melt synthesis.[34] A stable carbon-oxygen framework forms already at a temperature as low as 300 °C, as evidenced by forming a porous network with SSA of 658 m^2 g^{-1} measured by N_2 sorption (**Figure 3**a). However, structural ripening of the porous network was still possible. Interestingly, the isotherms for samples calcined between 400 and 800 °C remained nearly identical,

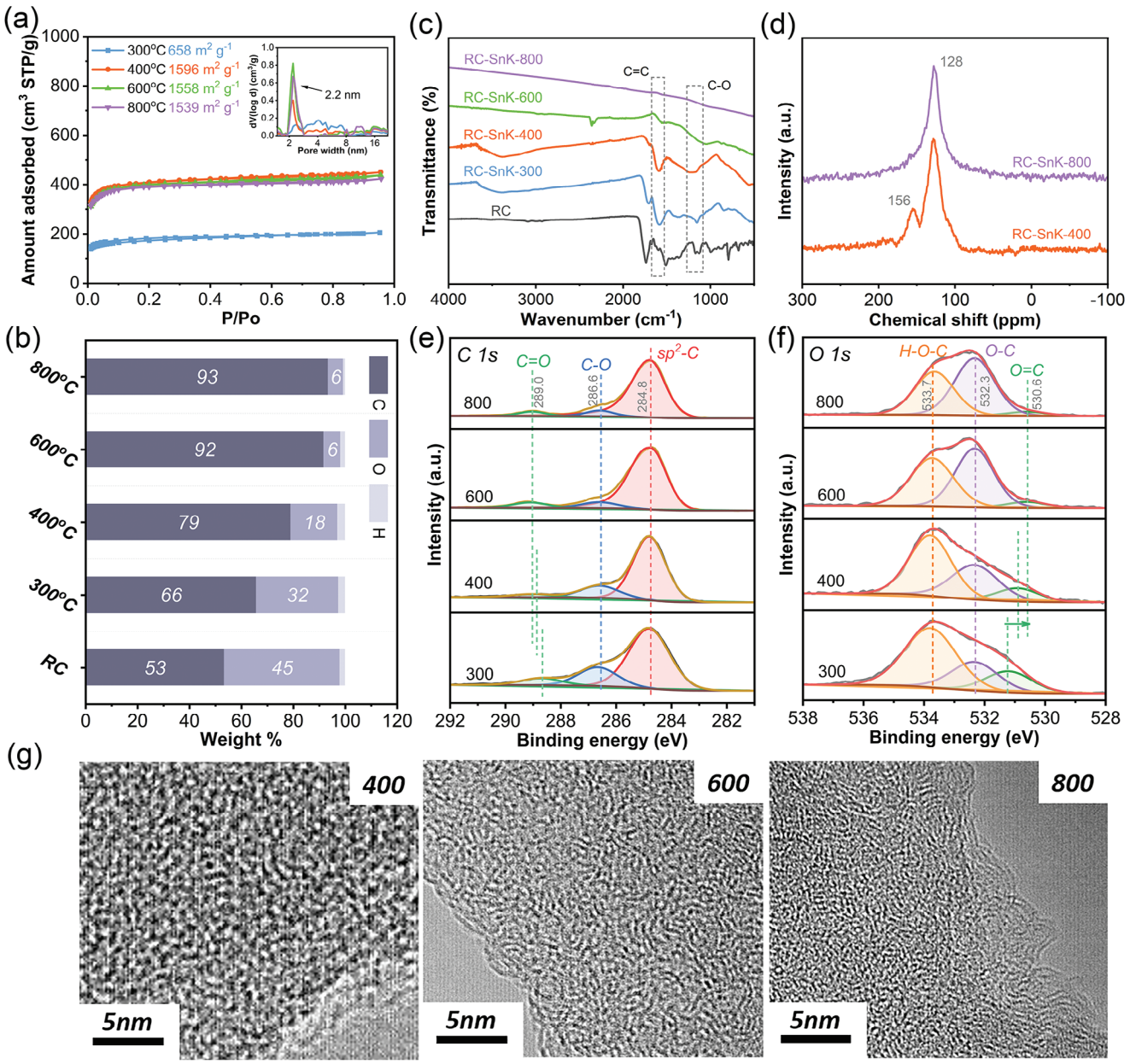

Figure 3. The influence of condensation temperature on carbon properties. a) N_2 adsorption–desorption isotherms at 77 K (inset: corresponding pore-size distributions calculated by QSDFT model from adsorption branch), b) elemental composition determined by ECA, and c) FTIR spectra of RC, RC-SnK-300, RC-SnK-400, RC-SnK-600, and RC-SnK-800; d) ^{13}C NMR spectra of RC-SnK-400, and 800; e) Deconvoluted C1s XPS spectra, and f) deconvoluted O1s XPS spectra of RC-SnK-300, RC-SnK-400, RC-SnK-600, and RC-SnK-800; g) HRTEM images of RC-SnK-400, RC-SnK-600, and RC-SnK-800.

exhibiting the SSA of ≈1600 $m^2 g^{-1}$ and a rather narrow pore size distribution with an average pore size of 2.2 nm. In addition, the CO_2 sorption isotherms at 273 K suggest the presence of narrow micropores (Figure S10, Supporting Information). Similarly, to N_2 sorption isotherms at 77 K, CO_2 isotherms are very similar between RC-SnK-400 and RC-SnK-800 (about 5 mmol g^{-1} of total uptake), confirming their equivalent porosity. This observation is noteworthy, as the structure and microstructure of carbonaceous materials typically evolve together at higher temperatures.[34] In this case, the mesostructure matured without modifying the microstructure.

The stability of the pore structure is surprising since the materials undergo significant chemical changes in this temperature range as reflected by the yield of the process (43.5% at 400 °C and 31.3% at 800 °C) and the chemical composition determined by elemental chemical analysis(ECA) (Figure 3b and Table S2, Supporting Information). RC-SnK-400 possesses 79 wt% of C and 18 wt% of O, while for RC-SnK-800, it is 93 and 6 wt%, respectively. The composition and mass changes are associated with the loss of oxygen functional group. Figure 3c displays the FTIR spectra of each sample correlated with the spectrum of the RC precursor. The broad character of the bands is a sign

of highly conjugated structures. The initially strong band from lactone, centered at 1740 cm^{-1}, vanished at 400 °C, pointing to the loss of carbonic ester groups. At the same time, the bands in the range of 1200–1000 cm^{-1} characteristic of C—O merged into one broadband indicative of C—O functionalities such as C—OH and C—O—C conjugated with aromatic domains. Another visible band at 400 °C is the one at 1587 cm^{-1} originating from C=C stretching. The bands disappear upon heating to 600 and 800 °C, demonstrating the loss of O and the presence of large conjugated domains. ^{13}C solid-state magic-angle spinning nuclear magnetic resonance spectroscopy (^{13}C MAS NMR) with direct polarization (DP) confirmed the FTIR results (Figure 3d). The sample calcined at 400 °C shows two peaks, one stronger at around 128 ppm, typical for sp^2 carbons not attached to any heteroatom, and the second weaker at 156 ppm, which can be assigned to sp^2 carbon atoms attached to one oxygen atom (either from hydroxide or ether).[35,36] Notably, the spectrum contains no signal from sp^3 carbons (20–60 ppm) and carbonyl groups (>170 ppm). All the oxygen atoms are thus fully conjugated with the sp^2 carbon network. At 800 °C, the peak at 156 ppm disappears, and only the broad peak at 128 ppm remains. Some residual carbons attached to oxygen might be hidden in the shoulder at higher ppm. Indeed, X-ray photoelectron spectroscopic (XPS) experiments detected residual oxygen atoms. All of the samples display similar XPS survey spectra with the signal of C1s and O1s without a peak of Sn 3d (Figure S11, Supporting Information). The C1s spectra of RC-SnK-300 and RC-SnK-400 displayed three main components centered at 284.8, 286.6, and 288.7 eV, assigned to sp^2-C, C—O, and C=O bonds, respectively (Figure 3e). However, as the temperature increased to 600 and 800 °C, a significant change occurred in the sp^2-C peak. It became broader and asymmetric, indicating the formation of larger conjugated carbon domains resulting from the loss of oxygen. A similar phenomenon was observed for graphene oxide heated to 1000 °C and compared to one heated at 250 °C.[37] Moreover, the asymmetry in RC-SnK-600 and RC-SnK-800 sp^2-C peaks suggested the presence of conductive carbon networks.[38] The peaks corresponding to C—O and C=O were still present but with significantly lower intensity, confirming the presence of oxygen functionalities even at 800 °C. Furthermore, the peak from C=O shifted to higher binding energies at higher temperatures. A similar trend was observed in the O1s spectra, where the peak corresponding to O=C initially located at 531.3 eV shifted toward lower binding energies (530.6 eV at 800 °C) (Figure 3f), meaning that electron density transferred from carbon to oxygen.[39] The O1s spectra contained other bands at 532.3 and 533.7 eV, corresponding to —C—O—C and H—O—C bonds, respectively. H—O—C dominated at 300 °C but gradually lost its intensity at higher temperatures making the peak from C—O—C more intense. This observation aligns with FTIR results, where the —OH groups were clearly visible above 3000 cm^{-1} up to 600 °C.

None of the samples showed translation order, as XRD diffractograms do not contain diffraction peaks (Figure S12, Supporting Information). Therefore, Raman spectroscopy was used to investigate the evolution of the carbon structure during thermal treatment (Figure S13, Supporting Information). Initially, the RC precursor displayed a single peak at 1513 cm^{-1}, which is the typical signal for polyacetylenes with alternating double bonds.[40,41] After heat treatment, each sample's spectrum displayed the typical signature of carbonaceous materials with bands commonly described as D- and G-bands and located at around 1345 and 1574 cm^{-1}, respectively. The G band became sharper at higher temperatures, while the D band shifted from 1363 to 1335 cm^{-1}. Both effects point to the formation of larger aromatic domains, or in other words, to a better in-plane organization of the carbon lattice,[42] as expected upon consecutive removal of oxygen atoms.

The SEM pictures of the precursor and materials prepared at different temperatures are shown in Figure S14, Supporting Information. Flat fragments appeared at 300 °C as irregular scraps, while larger and thinner flakes were generated at higher temperatures. The high-resolution (HR) TEM confirmed the results of the Raman analysis. The sample RC-SnK-400 demonstrated featureless images typical of disordered amorphous carbons. In contrast, the RC-SnK-600 and RC-SnK-800 revealed the graphenic domains of a few nanometers (Figure 3g).

At last, we studied the influence of the ratio between the precursor and the molten salt (from 1:1 to 1:50) for samples calcined at 400 °C. The results are presented and discussed in the Supporting Information (Figure S15, Supporting Information). Briefly, XRD, ECA, FTIR, and Raman analysis demonstrated that the difference between the samples was negligible for the ratios between 1:5 and 1:50.

2.4. Electrocatalytic NO_3^- Reduction

The electrochemical performance of RC-SnK-800 was initially assessed by conducting cyclic voltammetry (CV) experiments at different scanning rates in 1 M H_2SO_4 (Figure S16, Supporting Information). Even at fast scan rates of 500 mV s^{-1}, the CVs maintained their rectangular shape, indicating excellent sample conductivity. In addition, the appearance of redox peaks confirmed the presence of convertible oxygen functional groups on the surface of the material. The high surface area, conductivity, and presence of oxygen functional groups are suitable for electrocatalytic processes, as already shown in oxygen reduction reactions catalyzed by nanoporous carbons.[43–45] Carbon-based and metal-free electrocatalysts are especially important in applications where the leaching of metal electrodes is a serious drawback. This is the case in any water purification process.

Electrochemical nitrate reduction (NO_3RR) has emerged as a promising approach for converting the NO_3^- pollutant into harmless N_2 or valuable NH_3.[46,47] It also offers a more efficient alternative to the electrochemical generation of ammonia in comparison to electrochemical nitrogen reduction reactions.[48–50] The practical nitrate sources, such as wastewater, often exhibit low concentrations ranging from hundreds to thousands of ppm.[51] Achieving effective conversion under such conditions requires highly active catalysts that can enrich their high surface area with nitrates through specific interactions.[52] Carbon-based electrocatalysts are particularly attractive in this regard, as they can provide a high surface area and mitigate potential pollution associated with metal electrodes. However, carbon catalysts are often limited by their lower activity and selectivity compared to metals. In this study, we demonstrate that the developed nanoporous oxocarbons serve as excellent electrocatalysts for nitrate reduction to ammonia at low and high nitrate levels, exhibiting high ammonia yield production. This can be attributed to

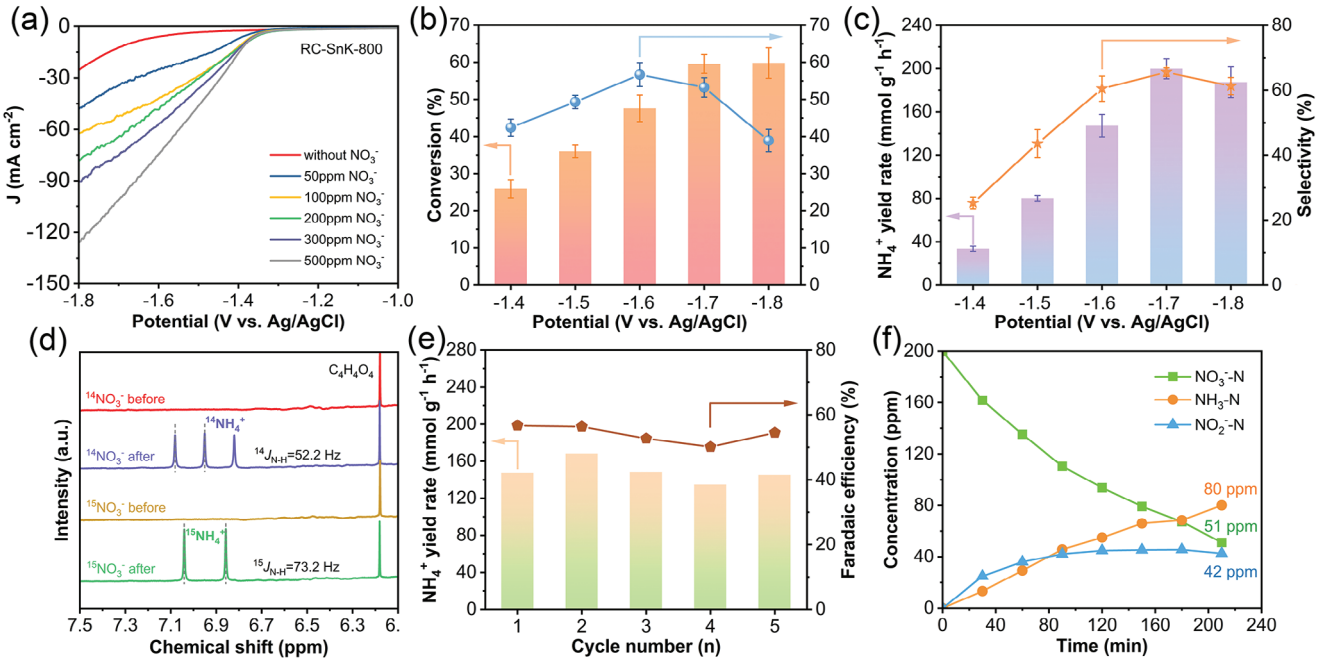

Figure 4. NO_3RR performance of RC-SnK-800 in 0.5 M Na_2SO_4 with 200 ppm NO_3^--N. a) LSV curves under different nitrate concentrations (scan rate: 10 mV s^{-1}); b) Conversion and FE determined using UV–vis spectroscopy, and c) NH_4^+ yield rate and selectivity determined using UV–vis spectroscopy after 2 h chronoamperometry tests under different potentials; d) ^{1}H NMR spectra of the electrolyte before and after NO_3RR using $^{15}NO_3^-$ or $^{14}NO_3^-$ as nitrogen reaction substrate, respectively; e) The consecutive stability measurements at −1.6 V; f) Time-dependent concentration change of NH_3-N, NO_3^--N, and NO_2^--N during chronoamperometry at −1.6 V.

their high overpotential for the competitive hydrogen evolution reaction (HER), the high surface area with oxygen functionalities, which facilitates nitrate enrichment at the carbon surface.[53]

The electrocatalytic nitrate reduction reaction was evaluated in an H-type electrolytic cell using 0.5 M Na_2SO_4 as an electrolyte and sodium nitrate with a concentration of 200 ppm NO_3^--N (the nitrogen content was calculated by using the unit of g g^{-1}). The working electrode was prepared by coating RC-SnK-800 on top of carbon paper. As depicted in **Figure** 4a, linear sweep voltammetry (LSV) shows that RC-SnK-800 displays a high overpotential for HER in 0.5 M Na_2SO_4 without nitrate. In contrast, an obvious increment of current density started from −1.3 V versus Ag/AgCl when adding nitrate to the electrolyte. The current density positively correlates with the increasing concentration of nitrate up to 500 ppm, reflecting the enhanced mass transfer at higher initial concentrations.[54] The control experiment on the bare carbon paper showed a much higher overpotential and lower current density toward the NO_3RR, confirming that the NO_3RR can be attributed to RC-SnK-800 (Figure S17, Supporting Information). We would like to point to the fact that our system reached, in such academic set-ups, current densities of up to 100 mA cm^{-2}, which is beyond other carbon electrocatalysts, especially at such low substrate concentrations. This clearly speaks not only for excellent electronic conductivity but also for substrate pre-binding and product release. Catalysts that can adsorb nitrate relatively strongly are more likely to be active in the process of $*NO_2^-$ formation, which is the rate-determining step of NO_3RR.[55,56]

Subsequently, chronoamperometry was run for 2 h under different potentials (Figure S18, Supporting Information). After that, the concentrations of reactants and products (nitrate and ammonia) were quantified by well-established colorimetric methods using UV–vis spectroscopy.[57] The calibration curves were prepared for each reactant as described in the Experimental Section in Supporting Information (Figures S19–S21) . From −1.4 to −1.8 V versus Ag/AgCl, the conversion of nitrate gradually increased from 26% to 60% due to increased driving force for NO_3RR, while the FE of ammonia exhibited a volcanic shape curve and reached the maximum value of 56.7% at −1.6 V versus Ag/AgCl (Figure 4b), pointing to charge consumption by the HER at more negative potentials. The evolved hydrogen gas bubbles not only occupy the electrocatalytic active sites but also impede ion transport, thereby inhibiting the NO_3RR.[58] The yield rate and selectivity toward ammonia increased from −1.4 to −1.7 V versus Ag/AgCl, reaching the highest values of 0.138 mmol cm^{-2} h^{-1} (199.7 mmol g^{-1} h^{-1}) and 65.6%, and then slightly declined at more reductive potentials (Figure 4c).

^{1}H nuclear magnetic resonance spectroscopy (^{1}H NMR) was also employed to quantify the concentration of the generated ammonia by using maleic acid as an internal standard. The typical triple peaks of NH_4^+ located at 6.85, 6.98, and 7.11 ppm confirmed the formation of ammonia (Figure S22, Supporting Information). Due to the relationship between the peak area and the content of NH_4^+, the concentration of ammonia can also be determined. Figure S23, Supporting Information, compares the NH_4^+ yield rate and FE of the electrocatalytic process calculated by NMR and UV–vis spectrometry. The two methods are in good accordance, which validates the reliability of the ammonia production quantification.

In order to further confirm that ammonia was electrochemically produced from nitrate solution rather than extraneous

nitrogenous contaminants, isotopic ^{15}N labeling experiments were carried out using $Na^{15}NO_3$ as a nitrate source. The electrolyte solutions were analyzed before and after chronoamperometry by ^1H NMR. ^1H NMR spectra after chronoamperometry depicted in Figure 4d show two peaks at 6.86 and 7.04 ppm, typically ascribed to $^{15}NH_4^+$, while no signal existed before the electrocatalytic process. This unambiguously proves that the electrochemical reduction of the labeled nitrate leads to ammonia. Additionally, after immersing the working electrode in the electrolyte for 2 h without applying any potential, the ^1H NMR pattern of the electrolyte displayed no signal of NH_4^+, which excludes the possibility of catalytic ammonia generation (Figure S24, Supporting Information). Besides, to further validate that the residual Sn has a minimal impact on the NO_3RR, we utilized commercial SnO_2 nanoparticles as a catalyst to perform the NO_3RR under the same measurement conditions. As depicted in Figure S25, Supporting Information, when using an equivalent loading mass of SnO_2 as RC-SnK-800, it demonstrated a significantly lower NH_4^+ yield rate (33.41 vs 147.3 mmol g^{-1} h^{-1} observed with RC-SnK-800). Considering the minute amount of Sn (0.08 wt%) present in the sample, it is evident that the activity of NO_3RR contributed by Sn species is negligible. Furthermore, the NH_4^+ yield rate and the FE present minor fluctuations during five consecutive cycles, indicating the excellent stability of the catalyst (Figure 4e).

The time-dependent concentration changes of the main reactants and products (ammonia, nitrate, and nitrite) and the performance stability were studied at the optimum potential of −1.6 V versus Ag/AgCl. As presented in Figure 4f, the nitrate concentration gradually decreased with time, while that of ammonia increased. Notably, the nitrite concentration significantly rises during the first hour and then stabilizes at a certain level of about 40 ppm and slightly declines after 3 h. The constant concentration of nitrite after the induction period demonstrates that the NO_3^- reduction to NO_2^- is a rate-determining step.[55,56] Nitrates were almost completely converted to ammonia and nitrite in the first 90 min, as the sum of all nitrogens is 199 ppm. Considering that the formation of NO_2^- is the intermediate product, the selectivity and FE approach near 100%. However, the total amount of nitrogen decreased at longer times, reaching 175 ppm after 3 h. The formation of other N compounds cannot explain the sudden drop, as no other product was formed in the first 90 min. Therefore, two scenarios are possible i) the evaporation of ammonia; ii) the diffusion of ammonia from the cathode to the anode compartment through the Nafion membrane. In fact, the diffusion of ammonia through the Nafion membrane has already been reported in the N_2RR experiments.[59]

The efficiency of nitrate removal and stability during a continuous prolongated process was further evaluated through complete nitrate electroreduction conducted at −1.6 V using the solution with 1307 ppm NO_3^--N. Notably, 96.4% nitrate conversion was achieved within 30 h. The initial high nitrate concentration ensured a sufficient substrate concentration to mitigate mass transfer limitations, even at high conversion values. Throughout the process, the ammonia yield rate and FE steadily increased, reaching a yield rate of 221 mmol g^{-1} h^{-1} and FE of 93.4% after 16 h (not including NO_2^-), and then declined because of the depletion of nitrate (**Figure 5a**). The concentration of ammonia, nitrate, and nitrite showed a similar trend to that observed at NO_3^--N concentration of 200 ppm (Figure S26, Supporting Information). While the nitrate and ammonia concentrations gradually decreased/increased almost linearly through most of the process, the nitrite concentration remained stable at ≈120 ppm (declining at the end of the process). In this experiment, the ammonia concentration was determined in both catholyte and anolyte. The amount of ammonia in anolyte increased from 2% to 10% of the overall ammonia amount, confirming our previous observations. In addition, some part of the ammonia was likely oxidized at the Pt electrode to N_2, reducing the total ammonia concentration. In the case of a solution with 200 ppm of NO_3^--N, almost complete conversion was achieved in 8 h with a steadily decreasing rate of the process (Figure S27, Supporting Information).

In addition, the performance of RC-SnK-400 was also evaluated for comparison. As shown in Figures S28 and S29, Supporting Information, RC-SnK-400 shows a lower ability to reduce nitrates from the solution compared to RC-SnK-800, but it is still competitive with other carbon materials, even some catalysts-supported metals (Table S3, Supporting Information). Figure 5b graphically compares the performance of obtained oxocarbons for nitrate electroreduction to ammonia with the carbon-based materials reported in the literature and listed in Table S3, Supporting Information, with the corresponding references. RC-SnK-800 shows a remarkable NH_3 yield rate in both 200 and 1307 ppm NO_3^--N, even higher than some Cu-containing catalysts, efficient NO_3^- removal (93.2% in 8 h for 200 ppm NO_3^--N and 96.4% in 30 h for 1307 ppm NO_3^--N), and high NH_3 FE reaching 93.4%.

The excellent performance of the RC-SnK-800 carbocatalyst in the NO_3RR process can be attributed to several factors. First, the catalyst exhibits high conductivity, as demonstrated in Figure S16, Supporting Information, which facilitates efficient charge transfer. To support that, we performed impedance spectroscopy. The Nyquist plot with the fitting equivalent circuit in Figure S30 and Table S4, Supporting Information, confirmed that the charge transfer resistance (R_{ct}) of RC-SnK-800 was much lower compared to that of RC-SnK-400 and pure carbon substrate. Moreover, RC-SnK-800 presents a much higher electrochemical active surface area (ECSA) that can be estimated by calculating double-layer capacitance (C_{dl}) with the value of 12.03 mF cm^{-2} compared to RC-SnK-400 (3.76 mF cm^{-2}), contributing to more exposed active sites for catalytic reactions (Figure S31, Supporting Information).

The substrate and product binding is crucial for optimizing the NO_3RR performance, especially in the case of its small concentration. Previous studies using cyclodextrin-based electrocatalysts have highlighted the significance of pre-binding nitrate with oxygen functionalities.[53] To study the adsorption ability of different carbons, we conducted tests on the NO_3^- adsorption capacity of RC-SnK-400, RC-SnK-800, and commercial activated carbon (AC, oxygen content < 4 wt%, SSA is ≈2000 m^2 g^{-1}). Each material was dispersed into an electrolyte of 0.5 M Na_2SO_4 containing 200 ppm NO_3^--N. After a 5-min and 2-h interaction, the catalysts were filtered, and the residual nitrate was quantified using UV–vis measurements. As illustrated in Figure 5c,d, RC-SnK-800 exhibited much higher adsorption capacity compared to AC and RC-SnK-400 after both 5 min and 2 h, effectively underscoring the significance of the interplay between a highly conjugated carbon network and the presence of oxygen functionalities in nitrate adsorption.

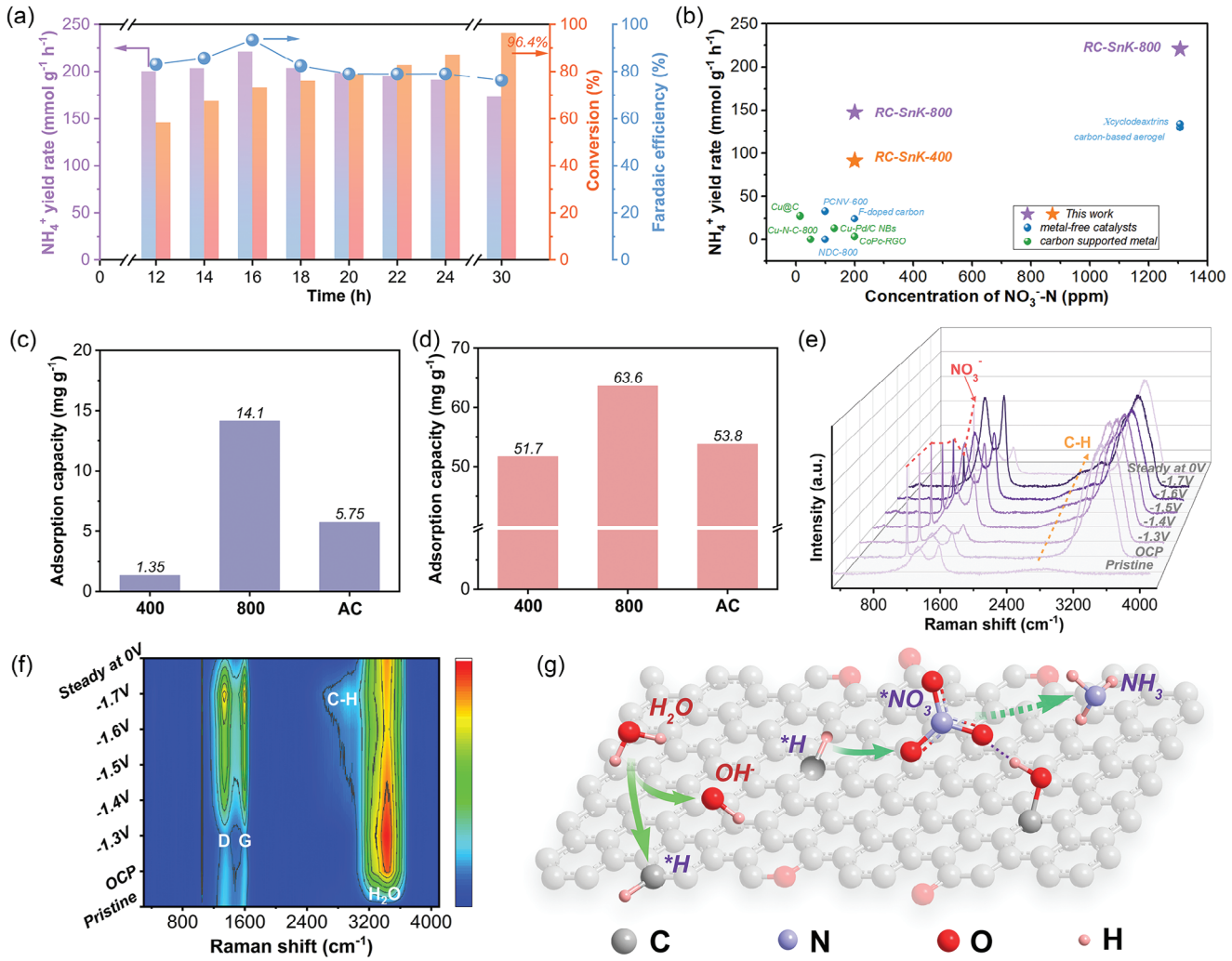

Figure 5. a) NH_4^+ yield rate, FE, and nitrate conversion during long-term chronoamperometry at −1.6 V in 0.5 M Na_2SO_4 with 0.1 M $NaNO_3$ (1307 ppm NO_3^--N); b) Performance comparison of NH_4^+ yield rate with metal-free catalysts and carbon supported metal in literature; nitrate adsorption capacities of RC-SnK-400, RC-SnK-800, and activated carbon after; c) 5 min and d) 2 h; e) In situ electrochemical Raman spectra of RC-SnK-800 for NO_3RR and f) corresponding heat map; g) Schematic illustration of the NO_3RR mechanism on RC-SnK-800.

In fact, it has been reported that the -OH groups can stabilize the adsorption of $*NO_x$ species owing to the hydrogen bonds.[60] A recent study by Cai et al.[61] also demonstrated that the favorable interaction of nitrate with —OH groups on OH-terminated MXenes was facilitated by hydrogen bonding. This interaction was found to play a pivotal role in adsorbing nitrates and their intermediates during reduction. Similarly, Dai et al.[53] attributed the notable activity of cyclodextrin-based cathodes to interactions through the mechanism likely involving hydrogen bonding. Hence, we posit that NO_3^- binds to our materials through the surface oxygen atoms via hydrogen bonding. The analyses showed that RC-SnK-800 contains two types of oxygen atoms, C—O and C═O. It is evident from XPS analysis that the carbonyl group undergoes a significant shift upon thermal treatment at elevated temperatures, signifying a transfer of electron density from carbon to oxygen atoms (Figure 3e,f). The resulting oxygen position approaches the value similar to oxygen atoms bound to metals. Consequently, the electronic properties of oxygen atoms, and thereby the strength of hydrogen bonding, depend on the conjugated carbon network. Notably, in solution, highly conjugated C═O groups transition through a tautomerization reaction, forming conjugated C—OH groups capable of proton bonding Alternatively, C═O groups can proton bond to nitrate through water molecules.

To study the mechanism of NO_3RR on RC-SnK-800, we carried out in situ Raman analysis, simultaneously examining the electrode and the electrolyte (1 M $NaNO_3$) from open circuit potential (OCP) to −1.7 V versus Ag/AgCl. As depicted in Figure 5e and Figure S32, Supporting Information, upon immersing the electrode in the electrolyte, characteristic vibration of aqueous NO_3^- emerged at 1049 cm^{-1},[62] and bands related to water over 3000 cm^{-1}. In addition, D and G bands from the RC-SnK-800 catalyst occur at 1345 and 1574 cm^{-1}. The NO_3^- peak gradually decreased upon cathodic polarization. Concomitantly, new bands between 2700 and 3000 cm^{-1} emerged, with growing intensity at larger polarization. These observations are indicative of nitrate

consumption, accompanied by the formation of C—H bonds on the catalyst surface resulting from the Volmer step of water reduction. The generated active hydrogen (*H) appears vital for NO_3RR. Upon removing the potential and leaving the system steady for 5 min, the peak intensities of NO_3^- were retained and C—H disappeared. Moreover, the D and G bands of the carbon structure present similar as before without intensity ratio and position changes, indicating the short-range order of carbons remained during the process, further showing the good stability of the catalyst for NO_3RR (Figure S33, Supporting Information).

The potential-dependent variations were better visualized by the heat map (Figure 5f). A clear set of changes are visible in the C–H bond region (≈2700–2900 cm^{-1}) and D (1345 cm^{-1}) and G bands (1574 cm^{-1}), while the signals characteristic for water (>3000 cm^{-1}) show only slight intensity reduction. Curiously, the D and G bands augmented with the applied potential, without a major change in the position or shape of the peaks. The increase might stem from structural changes, pressure induced by adsorbing counterions, or polarization enhancing bond polarizability and signal strength.[63] Alternatively, the newly observed C—H bands might influence the G and D band profiles or prompt structural rearrangements.[64] The peaks from water remained almost unchanged, with only a slight decrease in the intensity upon increasing potential. This might come from the consumption of water in the pores or from the expulsion of water from pores decorated with C—H bonds making it more hydrophobic.

To further investigate the presence of *H, the catalyst was deposited onto a glassy carbon electrode, and CV was conducted. The potential window ranged from the non-faradaic region to the hydrogen evolution region. As depicted in Figure S34, Supporting Information, within the potential range of −0.7 to 0.5 V versus Ag/AgCl, the catalyst predominantly exhibits capacitive behavior. On extending incrementally the potential window toward more negative values (up to −1.5 V vs Ag/AgCl), a pronounced reduction current associated with the HER is observed. Notably, during the scan to more positive potentials, an oxidation peak at ≈0.2 V versus Ag/AgCl intensifies and broadens as the potential window is expanded. This observation, which correlates with the oxidation of stored hydrogen,[65–67] indicates that *H is produced when applying a potential in a sufficiently negative region, essential for the nitrate reduction reaction NO_3RR to generate ammonia.

The coinciding consumption of NO_3^- and the appearance of C—H bonds suggest that the reduction follows the electrochemical hydrogenation route. This implies that the reduced proton (or water) on the carbon surface chemically interacts with NO_3^-. As a reducing agent, *H can efficiently break the N—O bonds.[25] The strong hydrogenation ability and efficient utilization of *H can suppress the competitive HER and enhance the FE and selectivity of the nitrate conversion.[24] Such a mechanism was recently described for metallic catalysts.[26,68] Most studies indicate a proton-coupled electron transfer over electrochemical hydrogenation.[69,70] There are two possible pathways: i) Langmuir–Hinshelwood, in which NO_3^- would be first adsorbed on the carbon surface; ii) Eley–Rideal, in which NO_3^- would recombine with *H without adsorbing on the surface. Given the substantial adsorption of NO_3^- on the surface of RC-SnK-800, it is inferred that surface-adsorbed nitrate reacts with *H. The subsequent query concerns the nature of *H transfer to NO_3^-—as a hydrogen atom or a proton-electron couple.[71]

As proposed in Figure 5g, the potential NO_3RR mechanism starts with NO_3^- binding to the carbon surface via hydrogen bonds. Upon cathodic polarization, water undergoes reduction to form *H, pivotal for the entire process. This adsorbed NO_3^- interacts with two *H units to form NO_2^-, which then dissolves and re-adheres for subsequent reduction phases leading to ammonia. This intricate interplay between nitrate, water, and carbon surface oxygen atoms, mediated by hydrogen bonds, warrants comprehensive future research to elucidate its ramifications.

3. Conclusion

In this study, we introduced $SnCl_2$ as a non-innocent salt melt for the synthesis of nanoporous oxocarbons. The use of $SnCl_2$ salt melts proved to be highly effective in condensing oxygen-rich molecules, owing to the strong affinity of Sn(II) for oxygen and its redox activity, which facilitates the extraction of oxygen from molecular precursors. As the model molecular precursor, we used an oligomer of carbon suboxide $(C_3O_2)_x$, the member carbon oxides family with conjugated ladder structure and no inactive C—H groups. The resulting deoxygenation process, accompanied by the reduction of carbon atoms, triggers the cross-linking of RC ribbons forming large 2D structures composed exclusively of sp^2 carbons and conjugated oxygen species already at temperatures as low as 300 °C. The rapid condensation of carbon and the concurrent formation of SnO_2 nanoparticles leads to the development of large nanoporosity. Notably, the structural evolution at higher temperatures leads to higher conjugation without changing the morphology and porosity.

The combination of high electrical conductivity, the presence of redox-active oxygen species, and a high overpotential for the HER endow the synthesized materials with excellent catalytic properties for nitrate electroreduction, overpassing other carbon-based catalysts. We attribute this phenomenon to the efficient bonding of nitrate through hydrogen bonds and electrochemical hydrogenation reaction on the electrode surface. In a model wastewater system, the synthesized materials exhibited a remarkably high NH_3 yield rate of 221 mmol h^{-1} g^{-1} with FE of 93.4%. This enabled the removal of 200 and 1307 ppm of NO_3^--N in 8 and 30 h, respectively, with removal efficiencies of 93.2% and 96.4% using a wastewater volume of 60 mL per 0.69 mg of catalyst.

Supporting Information

Supporting Information is available from the Wiley Online Library or from the author.

Acknowledgements

This work was supported by the Max Planck Society for financial support. M.O. acknowledges Alexander Von Humboldt Stiftung for financial support.

Open access funding enabled and organized by Projekt DEAL.

Conflict of Interest

The authors declare no conflict of interest.

Data Availability Statement

The data that support the findings of this study are available from the corresponding author upon reasonable request.

Keywords

electrocatalysis, nitrate reduction, oxo-carbon, red carbon, tin chloride

Received: November 2, 2023
Revised: December 8, 2023
Published online: December 28, 2023

[1] W. Tian, H. Zhang, X. Duan, H. Sun, G. Shao, S. Wang, *Adv. Funct. Mater.* **2020**, *30*, 1909265.
[2] J. Lee, J. Kim, T. Hyeon, *Adv. Mater.* **2006**, *18*, 2073.
[3] A. Stein, Z. Wang, M. A. Fierke, *Adv. Mater.* **2009**, *21*, 265.
[4] J. Yin, W. Zhang, N. A. Alhebshi, N. Salah, H. N. Alshareef, *Small Methods* **2020**, *4*, 1900853.
[5] Z. Heidarinejad, M. H. Dehghani, M. Heidari, G. Javedan, I. Ali, M. Sillanp, *Environ. Chem. Lett.* **2020**, *18*, 393.
[6] R. Walczak, B. Kurpil, A. Savateev, T. Heil, J. Schmidt, Q. Qin, M. Antonietti, M. Oschatz, *Angew. Chem., Int. Ed.* **2018**, *57*, 10765.
[7] X. Liu, N. Fechler, M. Antonietti, *Chem. Soc. Rev.* **2013**, *42*, 8237.
[8] X. Liu, M. Antonietti, *Carbon* **2014**, *69*, 460.
[9] Z. Yu, X. Wang, Y.-N. Hou, X. Pan, Z. Zhao, J. Qiu, *Carbon* **2017**, *117*, 376.
[10] K. Sakaushi, S. J. Yang, T.-P. Fellinger, M. Antonietti, *J. Mater. Chem. A* **2015**, *3*, 11720.
[11] J. Li, J. Kossmann, K. Zeng, K. Zhang, B. Wang, C. Weinberger, M. Antonietti, M. Odziomek, N. López-Salas, *Angew. Chem., Int. Ed.* **2023**, *62*, e202217808.
[12] N. Fechler, T.-P. Fellinger, M. Antonietti, *Adv. Mater.* **2013**, *25*, 75.
[13] X. Liu, M. Antonietti, *Adv. Mater.* **2013**, *25*, 6284.
[14] Z.-Y. Wu, S.-L. Xu, Q.-Q. Yan, Z.-Q. Chen, Y.-W. Ding, C. Li, H.-W. Liang, S.-H. Yu, *Sci. Adv.* **2018**, *4*, eaat0788.
[15] L. Wang, L. Wang, L. Zhang, H. Liu, J. Yang, *Trends Chem.* **2022**, *4*, 1135.
[16] C. Lv, J. Liu, C. Lee, Q. Zhu, J. Xu, H. Pan, C. Xue, Q. Yan, *ACS Nano* **2022**, *16*, 15512.
[17] T. Wang, X. Cao, H. Qin, L. Shang, S. Zheng, F. Fang, L. Jiao, *Angew. Chem., Int. Ed.* **2021**, *60*, 21237.
[18] A. Cardoso, S. Neves, M. Da Silva, *Energies* **2008**, *1*, 79.
[19] A. Kundu, S. Prabhakar, M. Vairamani, S. Roy, *Organometallics* **1997**, *16*, 4796.
[20] Q.-R. Li, C.-Z. Gu, H. Yin, *Chin. J. Chem.* **2006**, *24*, 72.
[21] M. Odziomek, P. Giusto, J. Kossmann, N. V. Tarakina, J. Heske, S. M. Rivadeneira, W. Keil, C. Schmidt, S. Mazzanti, O. Savateev, L. Perdigón-Toro, D. Neher, T. D. Kühne, M. Antonietti, N. López-Salas, *Adv. Mater.* **2022**, *34*, 2206405.
[22] Z.-Y. Wu, M. Karamad, X. Yong, Q. Huang, D. A. Cullen, P. Zhu, C. Xia, Q. Xiao, M. Shakouri, F.-Y. Chen, J. Y. Kim, Y. Xia, K. Heck, Y. Hu, M. S. Wong, Q. Li, I. Gates, S. Siahrostami, H. Wang, *Nat. Commun.* **2021**, *12*, 2870.
[23] X.-F. Cheng, J.-H. He, H.-Q. Ji, H.-Y. Zhang, Q. Cao, W.-J. Sun, C.-L. Yan, J.-M. Lu, *Adv. Mater.* **2022**, *34*, 2205767.
[24] H. Luo, S. Li, Z. Wu, Y. Liu, W. Luo, W. Li, D. Zhang, J. Chen, J. Yang, *Adv. Mater.* **2023**, *35*, 2304695.
[25] H. Zhang, C. Wang, H. Luo, J. Chen, M. Kuang, J. Yang, *Angew. Chem., Int. Ed.* **2023**, *62*, 202217071.
[26] F. Zhang, J. Luo, J. Chen, H. Luo, M. Jiang, C. Yang, H. Zhang, J. Chen, A. Dong, J. Yang, *Angew. Chem., Int. Ed.* **2023**, *62*, 202310383.
[27] Y. Hattori, S. Mukasa, H. Toyota, H. Yamashita, S. Nomura, *Surf. Coat. Technol.* **2012**, *206*, 2140.
[28] P. Wang, F. Chang, W. Gao, J. Guo, G. Wu, T. He, P. Chen, *Nat. Chem.* **2017**, *9*, 64.
[29] N. Lopez-Salas, J. Kossmann, M. Antonietti, *Acc. Mater. Res.* **2020**, *1*, 117.
[30] M. S. Holt, W. L. Wilson, J. H. Nelson, *Chem. Rev.* **1989**, *89*, 11.
[31] R. G. Pearson, *J. Chem. Educ.* **1968**, *45*, 581.
[32] K. P. Kepp, *Inorg. Chem.* **2016**, *55*, 9461.
[33] J. Pirnat, J. Luznik, Z. Trontelj, V. Kaucic, *J. Chem. Phys.* **1982**, *76*, 2585.
[34] J. Kossmann, T. Heil, M. Antonietti, N. López-Salas, *ChemSusChem* **2020**, *13*, 6643.
[35] A. S. Mazur, M. A. Vovk, P. M. Tolstoy, *Fullerenes, Nanotubes, Carbon Nanostruct.* **2020**, *28*, 202.
[36] J. F. Waters, W. R. Likavec, W. M. Ritchey, *J. Appl. Polym. Sci.* **1994**, *53*, 59.
[37] R. Blume, D. Rosenthal, J.-P. Tessonnier, H. Li, A. Knop-Gericke, R. Schlögl, *ChemCatChem* **2015**, *7*, 2871.
[38] H. Estrade-Szwarckopf, *Carbon* **2004**, *42*, 1713.
[39] Z. Tian, N. Fechler, M. Oschatz, T. Heil, J. Schmidt, S. Yuan, M. Antonietti, *J. Mater. Chem. A* **2018**, *6*, 19013.
[40] H. E. Schaffer, R. R. Chance, R. J. Silbey, K. Knoll, R. R. Schrock, *J. Chem. Phys.* **1991**, *94*, 4161.
[41] H. Shirakawa, T. Ito, S. Ikeda, *Polym. J.* **1973**, *4*, 460.
[42] D. B. Schuepfer, F. Badaczewski, J. M. Guerra-Castro, D. M. Hofmann, C. Heiliger, B. Smarsly, P. J. Klar, *Carbon* **2020**, *161*, 359.
[43] G. V. Fortunato, M. S. Kronka, E. S. F. Cardoso, A. J. Dos Santos, A. C. Roveda, F. H. B. Lima, M. Ledendecker, G. Maia, M. R. V. Lanza, *J. Catal.* **2022**, *413*, 1034.
[44] D.-W. Wang, D. Su, *Energy Environ. Sci.* **2014**, *7*, 576.
[45] M. Jerigová, M. Odziomek, N. López-Salas, *ACS Omega* **2022**, *7*, 11544.
[46] M. Duca, M. T. M. Koper, *Energy Environ. Sci.* **2012**, *5*, 9726.
[47] Z. Jiang, Y. Wang, Z. Lin, Y. Yuan, X. Zhang, Y. Tang, H. Wang, H. Li, C. Jin, Y. Liang, *Energy Environ. Sci.* **2023**, *16*, 2239.
[48] R. Jia, Y. Wang, C. Wang, Y. Ling, Y. Yu, B. Zhang, *ACS Catal.* **2020**, *10*, 3533.
[49] Y. Wang, W. Zhou, R. Jia, Y. Yu, B. Zhang, *Angew. Chem., Int. Ed.* **2020**, *59*, 5350.
[50] J. Zhou, M. Wen, R. Huang, Q. Wu, Y. Luo, Y. Tian, G. Wei, Y. Fu, *Energy Environ. Sci.* **2023**, *16*, 2611.
[51] Y. Fernández-Nava, E. MaraN, J. Soons, L. Castrillón, *Bioresour. Technol.* **2008**, *99*, 7976.
[52] F. Lv, M. Sun, Y. Hu, J. Xu, W. Huang, N. Han, B. Huang, Y. Li, *Energy Environ. Sci.* **2023**, *16*, 201.
[53] X. Dai, L. Tian, Z. Liu, W. Xu, Y.-P. Liu, Y. Liu, *ACS Nano* **2022**, *16*, 18398.
[54] H. Xu, J. Wu, W. Luo, Q. Li, W. Zhang, J. Yang, *Small* **2020**, *16*, 2001775.
[55] X. Lu, H. Song, J. Cai, S. Lu, *Electrochem. Commun.* **2021**, *129*, 107094.
[56] Z. Wang, D. Richards, N. Singh, *Catal. Sci. Technol.* **2021**, *11*, 705.
[57] E. W. Rice, L. Bridgewater, A. P. H. Association, *Standard Methods for the Examination of Water and Wastewater*, American Public Health Association, Washington, DC, **2012**.
[58] W. Duan, G. Li, Z. Lei, T. Zhu, Y. Xue, C. Wei, C. Feng, *Water Res.* **2019**, *161*, 126.
[59] Y. Ren, C. Yu, X. Tan, X. Han, H. Huang, H. Huang, J. Qiu, *Small Methods* **2019**, *3*, 1900474.
[60] S. Tang, Z. Cao, *J. Chem. Phys.* **2011**, *134*, 044710.
[61] J. Cai, J. Huang, A. Cao, Y. Wei, H. Wang, X. Li, Z. Jiang, G. I. N. Waterhouse, S. Lu, S.-Q. Zang, *Appl. Catal., B* **2023**, *328*, 122473.
[62] W. Gao, K. Xie, J. Xie, X. Wang, H. Zhang, S. Chen, H. Wang, Z. Li, C. Li, *Adv. Mater.* **2023**, *35*, 2202952.

[63] S. Gupta, M. Hughes, A. H. Windle, J. Robertson, *J. Appl. Phys.* **2004**, *95*, 2038.
[64] A. Kaniyoor, S. Ramaprabhu, *AIP Adv.* **2012**, *2*, 032183.
[65] K. Jurewicz, E. Frackowiak, F. BeGuin, *Electrochem. Solid-State Lett.* **2001**, *4*, A27.
[66] K. Jurewicz, E. Frackowiak, F. Béguin, *Appl. Phys. A* **2004**, *78*, 981.
[67] S. Leyva-García, E. Morallón, D. Cazorla-Amorós, F. Béguin, D. Lozano-Castelló, *Carbon* **2014**, *69*, 401.
[68] K. Fan, W. Xie, J. Li, Y. Sun, P. Xu, Y. Tang, Z. Li, M. Shao, *Nat. Commun.* **2022**, *13*, 7958.
[69] K. Koh, U. Sanyal, M.-S. Lee, G. Cheng, M. Song, V.-A. Glezakou, Y. Liu, D. Li, R. Rousseau, O. Y. Gutiérrez, A. Karkamkar, M. Derewinski, J. A. Lercher, *Angew. Chem., Int. Ed.* **2020**, *59*, 1501.
[70] G. Cioncoloni, I. Roger, P. S. Wheatley, C. Wilson, R. E. Morris, S. Sproules, M. D. Symes, *ACS Catal.* **2018**, *8*, 5070.
[71] U. Roland, T. Braunschweig, F. Roessner, *J. Mol. Catal. A: Chem.* **1997**, *127*, 61.